

## 2 A pipeline for quantification of membrane and cytoplasmic protein concentrations

Intro to section, build on narrative from previous section

### 2.1 Autofluorescence correction

*Note: this section has been adapted from Rodrigues et al. (2022), and describes work performed with Nelio Rodrigues.*

#### 2.1.1 Autofluorescence in *C elegans*

One major barrier in quantitative experiments using *C. elegans* is autofluorescence (AF), which is particularly prominent in channels excited with blue wavelengths which are commonly used to image green fluorophores. When using endogenously tagged proteins, which are often expressed at low levels, this contribution can often be a significant fraction of the total signal, and can therefore significantly obscure the true signal that one is interested in. This might pose particular problems for quantitative experiments, where the absolute signal levels may be important.

We can observe the significance of the problem in *C. elegans* by imaging untagged control embryos. As shown in fig. 2.1 (left panels), a significant amount of signal is collected in the regular GFP channel (488nm excitation, 535/50nm emission), which varies both spatially within the image, and between different images. By comparison, total signal in embryos endogenously tagged with LGL-1::GFP ( fig. 2.1, right panels) is also highly variable, and only marginally higher than N2s, suggesting that a significant fraction of the total signal ob-

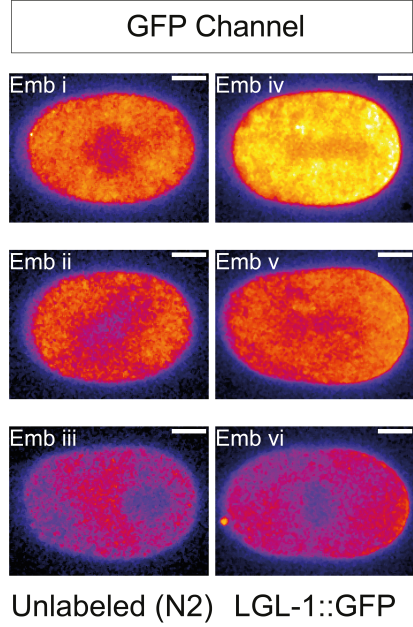


**Figure 2.1:** Autofluorescence is abundant and variable in images of *C. elegans* zygotes. GFP channel (488nm excitation, 535/50nm emission) images of unlabelled N2 and LGL-1::GFP embryos taken under identical imaging conditions. Pixel scaling is the same for each image. Fig. 1B from Rodrigues et al. (2022).

served in these cells is autofluorescence, and that much of the intra-embryo signal variation is likely due to variable autofluorescence. Despite being enriched at the posterior membrane, which is easily visible in cells with overexpressed LGL-1 (e.g. Hoege et al., 2010), this is difficult to visualise here as a result of autofluorescence. Therefore, if we want to accurately visualise, and indeed quantify, protein levels and distributions, we need a method that can locally correct AF on a pixel-by-pixel basis.

One approach that has been used to tackle autofluorescence in some systems is spectral imaging (Billinton and Knight, 2001). Typically used to separate overlapping fluorophore signals based on spectral characteristics, this approach can also be used to separate out autofluorescence by treating it much like a fluorophore with its own spectral characteristics. Whilst often effective, these techniques require specialised instruments and analysis tools and cannot be performed on standard confocal microscopes.

A simpler, related, approach has been proposed for some systems (e.g. Roederer and Murphy, [1986]) which exploits the fact that autofluorescence can often be described as a single fluorescent component, with an emission spectrum much broader than GFP. If one can find an emission wavelength (usually red shifted) that is specific for autofluorescence, this can be used to infer the amount of autofluorescence in the sample, which can then be subtracted away from the regular fluorophore channel to give a clean readout of fluorophore signal. In comparison to full spectral imaging, this method can be carried out with standard light sources and emission filters, and therefore can be easily implemented into existing workflows.

Inspired by this approach, we aimed to implement, and assess the applicability of such a method for autofluorescence removal in images of *C. elegans* embryos. In doing so, we have put together a robust and easily-implementable workflow which we've termed SAIBR: Spectral Autofluorescence Image correction by Regression.

### **2.1.2 SAIBR: a simplified method for autofluorescence correction based on dual emission imaging**

At minimum, autofluorescence correction relies on the ability to find a reporter channel that is free of GFP signal, but rich in autofluorescence, such that this channel can be used as an independent readout of autofluorescence in the sample. Full spectral analysis performed by Nelio Rodrigues (not shown here), shows that a channel with a red shifted emission filter, such as those

commonly used to image red fluorescent proteins, meets such a requirement.

Furthermore, by imaging untagged embryos with both the standard GFP channel and this red-shifted autofluorescence-reporter channel (488nm excitation, 630/75nm emission), which I will refer to as the AF channel, we find a strong linear correlation between pixel data from the two channels (fig. 2.2). Whilst raw pixel values do not correlate well, as these are dominated by noise, we can get a strong correlation by first applying a Gaussian filter to suppress this noise (fig. 2.2A). We found that this relationship is consistent between embryos (fig. 2.2B, C). Furthermore, we found a near identical relationship when plotting the mean intensity values of individual embryos, suggesting that the same relationship can account for both intra- and inter-embryo AF variation.

Together, this implies that taking an AF channel image should be sufficient to accurately predict the level of autofluorescence in the GFP channel, and thus subtract it out. To quantify the necessary inter-channel conversion factors, I performed linear regression, using an ordinary least squares method, on Gaussian-filtered pixel values pooled from multiple untagged embryos. Then, to perform correction on images containing fluorophore, we just need to capture an AF channel image, alongside the GFP channel image, rescale the AF image according to the predefined conversion factors, and then subtract this inferred autofluorescence away from the GFP channel image pixel-by-pixel.

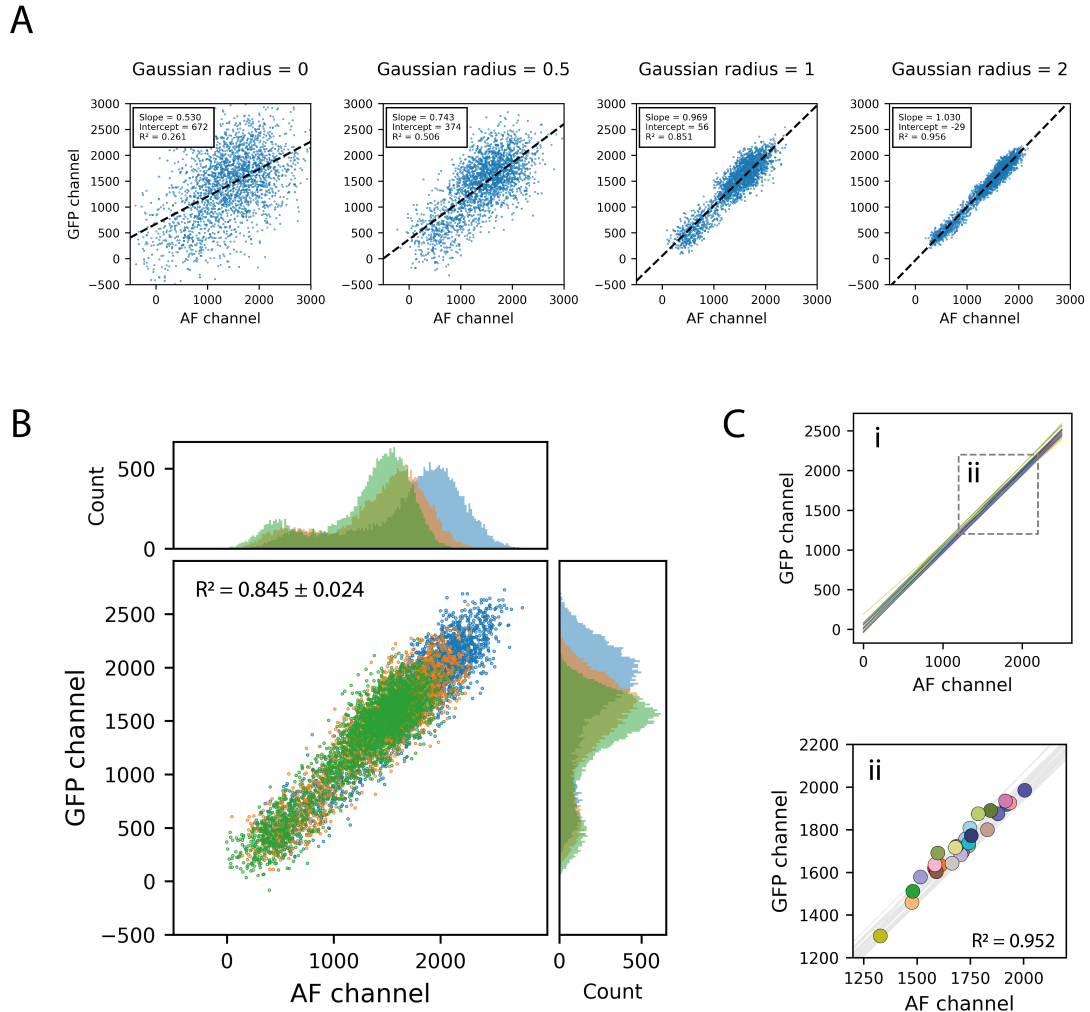


**Figure 2.2: Autofluorescence is spatially correlated across emission channels.** (A) Correlation of pixel values between the GFP channel and AF channel for an unlabelled N2 embryo, subject to Gaussian blur of indicated radius. Pixel values were taken from an ROI encompassing the entire embryo and a portion of the background. All pixels within this region were used for the regression, but for clarity only a random 10% sample of pixels are shown. (B) Comparison of inter-channel pixel correlation (Gaussian radius = 1) for three unlabelled N2 embryos, colour coded by embryo. Histograms of intensity values for GFP and AF channels shown for reference. (C) Comparison of per-pixel correlation with data obtained from whole embryo means. (i) Lines indicate per-pixel regression for individual embryos as in (B). (ii) Overlay showing mean whole embryo fluorescence values (circles). Fig. S2 and 1E-F from Rodrigues et al. (2022).

### 2.1.3 Assessing SAIBR performance on images of PAR proteins

To assess the effectiveness of SAIBR, and its utility in the analysis of PAR proteins, I applied it to a range of images of unlabelled and GFP-labelled embryos. As expected, applying SAIBR to images of unlabelled cells reduced fluorescence from across the cells to zero, with no visible structures remaining (fig. 2.3A). This is a good validation of the method, and suggests that it can properly account for all of the autofluorescence in the cell.

In the case of LGL-1::GFP expressing embryos, where autofluorescence signal is dominant (fig. 2.1), SAIBR removes autofluorescence signal within the cell, and improves contrast at the posterior cortex, allowing us to better resolve plasma membrane enrichment fig. 2.3B. Improvements are just as striking for PAR-3::GFP. In addition to improvements at the cortex, we see that SAIBR can suppress the local fluorescence minimum at the cell centre caused by lower AF at the pronuclei. For PAR-6::GFP the improvements are qualitatively less striking, as the ratio of fluorophore signal to autofluorescence is higher, but nonetheless AF removal has a quantitative impact.

As shown in fig. 2.4, SAIBR has a strong impact on the shape of intensity profiles taken across the cortex within each polarity domain, in all cases showing a clearer peak and suppression of signal at the internal portion of the curves. This has particular importance for quantitative studies as, as described in section 2.2, the shape of cross-cortex profiles are often used to quantitatively analyse membrane concentrations and/or membrane affinities. For example, a cross-cortex profile with a central peak that is much higher than the internal cytoplasmic plateau clearly implies that the protein is binding to the mem-

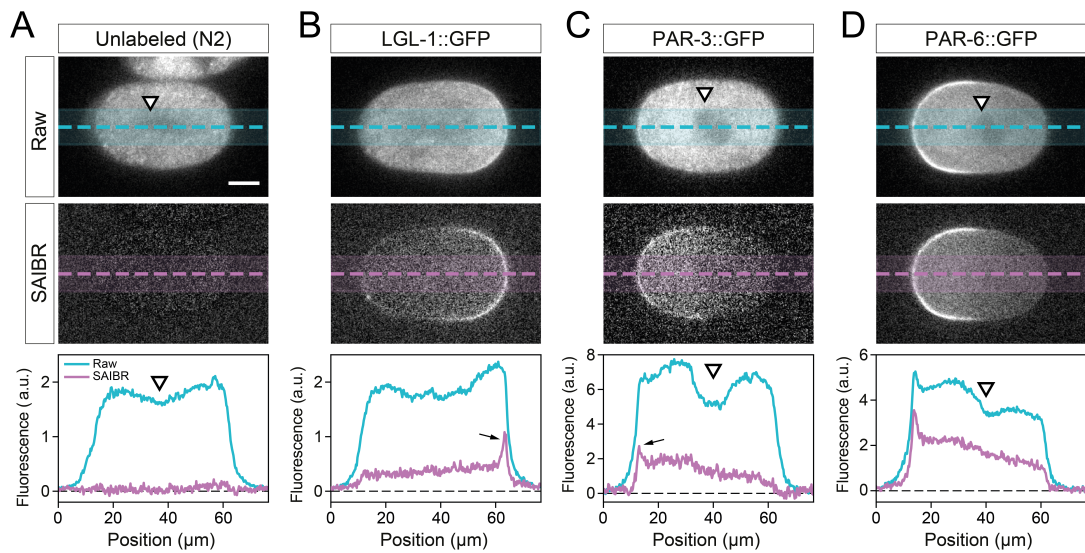


**Figure 2.3: Applying SAIBR to images of GFP-tagged PAR proteins.** (A) - (D) Raw (top) and SAIBR-corrected (middle) midplane images of zygotes expressing the indicated GFP fusions. Bottom panels show associated linescans across the images. SAIBR reveals prominent membrane localisation for LGL-1 and PAR-3 (arrows) which is not obvious in uncorrected images. We also see a prominent signal dip in the pronuclear region of uncorrected images due to local exclusion of autofluorescence (arrowheads), which disappears in SAIBR corrected images. Fig. 2A-D from Rodrigues et al. (2022).

brane with a high affinity. We can see from the SAIBR corrected profiles that, of the three proteins shown here, LGL-1 has the strongest membrane affinity (highest enrichment at the membrane compared to its cytoplasmic level), followed by PAR-6, followed by PAR-3. If we look at the profiles pre-correction, however, this isn't so clearly apparent. One might have had some success by simply subtracting an equivalent average profile taken from untagged N2s, but such a method would fail to account for the fact that much of variation between embryos is down to autofluorescence, and would therefore be unsuitable for studies where inter-embryo variation is important. In the case of LGL-1 this would also clearly result in negative values at the cytoplasmic portion of the curve for some embryos.

#### 2.1.4 Extending SAIBR to dual-labelled *C elegans* embryos

As SAIBR relies on a red shifted emission channel, complications can arise in samples containing red fluorophore. As red fluorophores are usually weakly excited by blue lasers, they will contribute additional signal to the AF channel, which may lead to overestimation, and therefore oversubtraction, of autofluorescence if not accounted for. If RFP levels are low, this effect may be small and can be ignored. However, if RFP levels are high, this bleedthrough effect can be significant. This can be demonstrated by observing the inter-channel relationship in control embryos expressing mCh::MEX-5 (fig. 2.5A). We find that, when an RFP is present, this relationship deviates significantly from the typical relationship observed in N2s, in direct proportion to local signal in the RFP (561nm excitation, 630/75nm emission) channel (fig. 2.5A inset). As this relationship is linear, autofluorescence in the GFP channel can be described

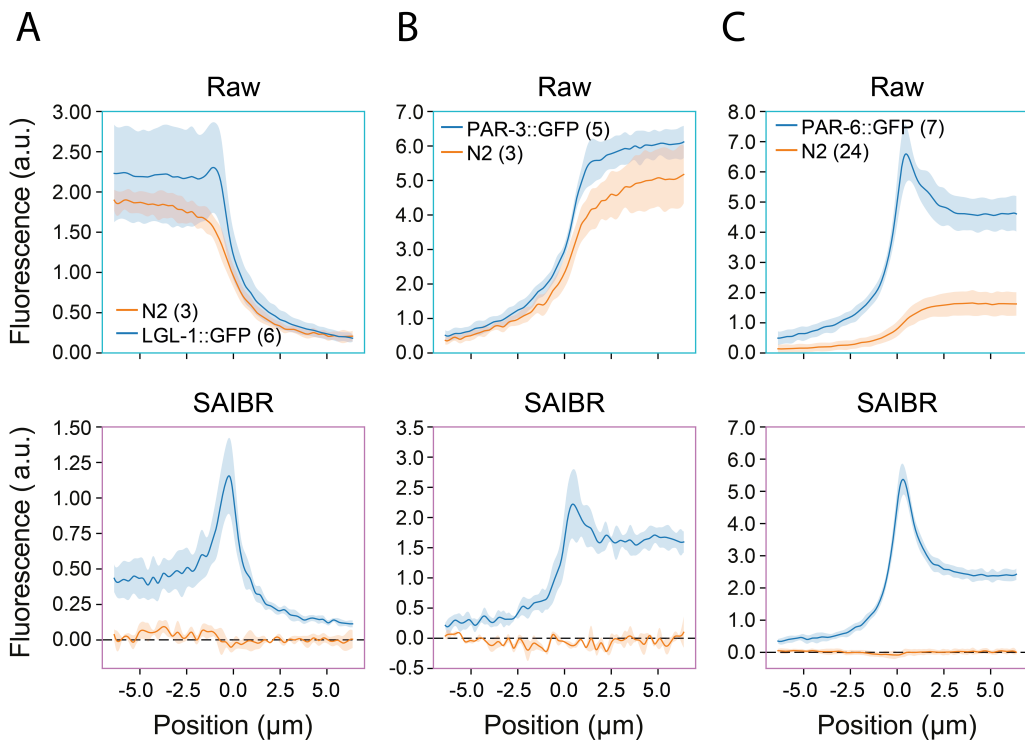


**Figure 2.4: SAIBR improves detection of membrane signals.** (A) - (C) Averaged membrane profiles taken from raw (top) and SAIBR-corrected (bottom) images for LGL-1::GFP (A), PAR-3::GFP(B) and PAR-6::GFP (C) shown relative to unlabelled N2 controls. Membrane position at  $x=0\mu\text{m}$ . Mean  $\pm$  SD indicated. Fig. 2E-G from Rodrigues et al. (2022).

as a linear function of both the AF and the RFP channels. Plotting pixel data in three dimensions shows that the data can be successfully fit to a plane, by performing multiple linear regression (fig. 2.5B, C).

To perform correction on images containing red fluorophore, we just need to capture all three channels, calculate autofluorescence using the three-channel regression relationship obtained from the appropriate RFP-tagged single line, and then subtract this away from the GFP channel image. This is demonstrated in fig. 2.6, for embryos expressing both PAR-6::GFP and mCh::MEX-5, or just mCh::MEX-5. Whereas 2-channel SAIBR results in oversubtraction of autofluorescence (particularly visible in the mCh::MEX-5 single line), this is eliminated when using 3-channel SAIBR.

### 2.1.5 Discussion

In summary, I have demonstrated that a simple protocol, which weve termed SAIBR, can be used to successfully remove autofluorescence in images of *C. elegans* zygotes. The improvements are particularly striking for images of fusion proteins with low levels of expression, such as LGL-1::GFP, but even in cases where expression levels are higher, AF correction will prove important for quantitative analysis of membrane concentrations, as discussed in the next section. For the rest of this thesis, unless otherwise stated, green fluorophore images will be presented with autofluorescence removed by SAIBR.

The simplicity of the method means that it can be easily incorporated into existing workflows, and should be applicable to a variety of imaging platforms.

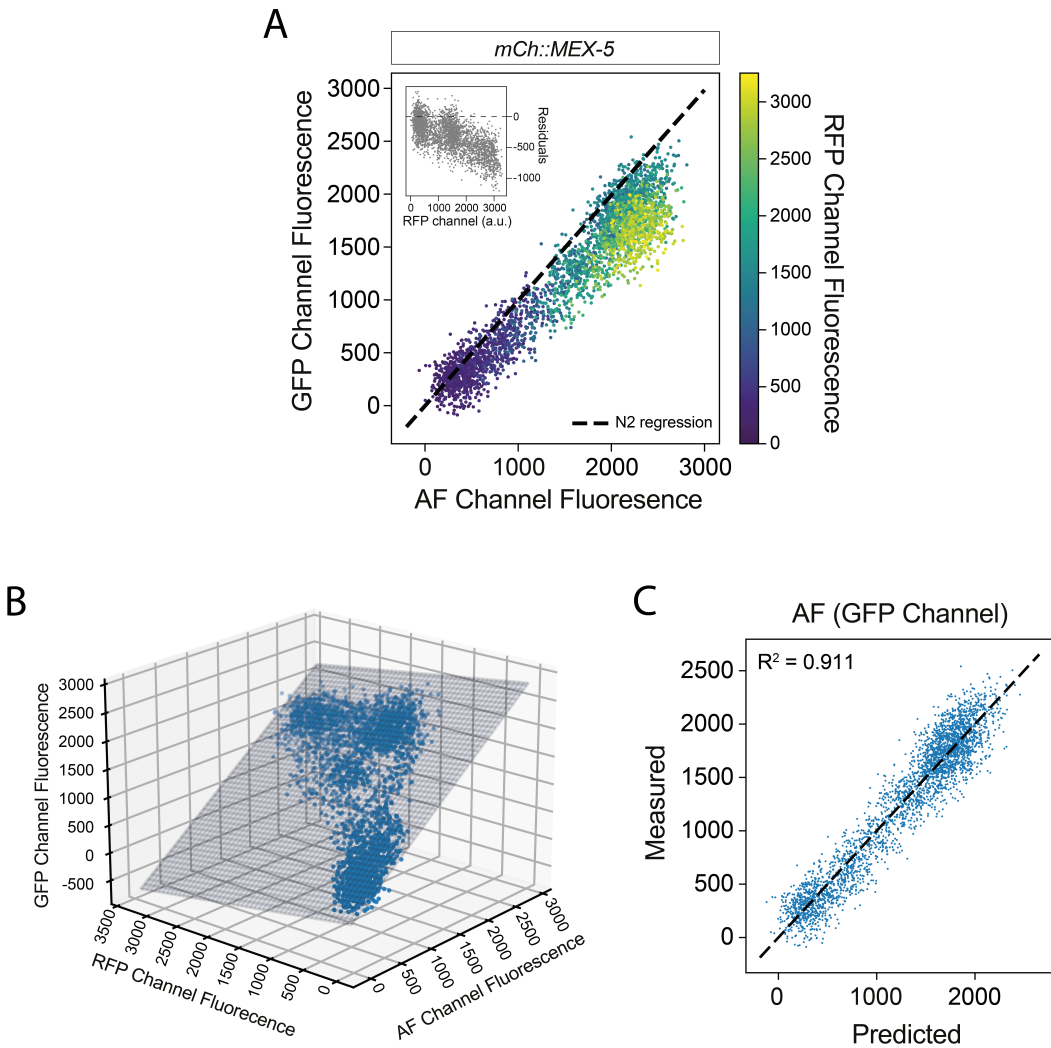


**Figure 2.5: Pixel intensities correlate across three channels in samples containing red fluorophore..** (A) Gaussian-filtered (radius = 1) GFP channel vs AF channel pixel intensities for an *mCh::MEX-5* expressing embryo, colour coded by RFP-channel fluorescence. Dashed line indicates the AF vs GFP correlation for untagged (N2) embryos. Inset shows residuals as a function of RFP channel signal. Pixels taken from an ROI encompassing the embryo and a region of the background, and 10% of pixels are shown at random. (B) Multiple regression fit of GFP-channel signal as a function of AF and RFP channel signal. The same embryo and sample of pixels as in (A) is shown. (C) Predicted vs. measured GFP-channel signal based on the fit in (B). The same embryo and sample of pixels as in (A) and (B) is shown. Fig. 4B-D from Rodrigues et al. (2022).

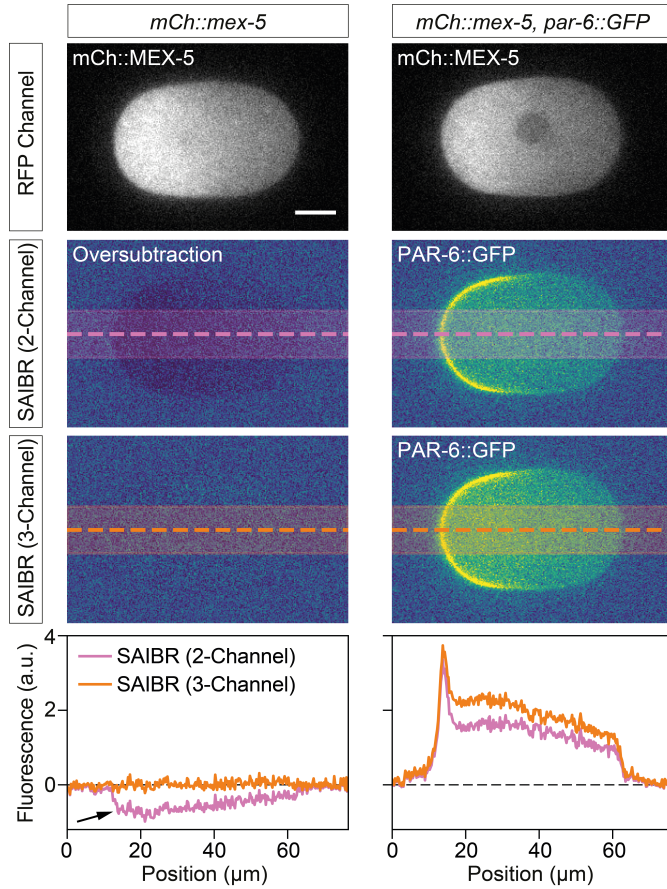


**Figure 2.6:** 3-channel SAIBR prevents oversubtraction in samples containing red fluorophore. RFP channel, 2-channel SAIBR and 3-channel SAIBR images for samples expressing *mCh::MEX-5*, along with associated linescans. 2-channel SAIBR results in oversubtraction which is clearly visible as negative values in the *mCh::MEX-5* line (arrow) and reduced cytoplasmic signal in the two-colour line. 3-channel SAIBR, using the calibration procedure shown in fig. 2.5, prevents oversubtraction. Fig. 4F from Rodrigues et al. (2022).

In the full study (Rodrigues et al., 2022), we show that the method is equally successful on both spinning-disk confocal and wide-field instruments.

Whilst initially developed with *C. elegans* embryos in mind, the method isn't specific to this system, and could be applied to a number of other model systems in which autofluorescence is a problem. In the full study, we show that the method works successfully in *C. elegans* larvae, as well as other model organisms such as starfish and yeast. That said, the method isn't guaranteed to perform well in all cases. If samples contain multiple, independently varying sources of autofluorescence, then SAIBR may face problems as a single autofluorescence reporter channel cannot account for this. However, much like how we can tackle red fluorophores, we have found that in some cases this can be solved simply by adding one extra reporter channel. Inevitably, though, such an approach may not be compatible with dual-colour imaging.

Whilst the analysis steps are relatively straightforward, implementing the computational workflow may still be a barrier to adoption for some. Therefore, to make the protocol accessible, I have put together a simple GUI-based FIJI plugin which can carry out all the necessary analysis in a few simple steps. This can be found here: [https://github.com/tsmbland/saibr\\_fiji\\_plugin](https://github.com/tsmbland/saibr_fiji_plugin).

The method comes with a few tradeoffs, which will vary in significance depending on the particular study. One issue is that, as the method combines pixel noise from multiple images, corrected images can in some cases be quite noisy, particularly where weak imaging conditions are used. It also requires capturing two emission channels for each image, which doubles sample illumination times and potential phototoxicity, which may be an issue for long

timelapses. Additionally, if samples display rapid motion, then the time lag between taking these two channels may lead to pixel mismatches, which could introduce artefacts. These last points could be fixed by using an imaging setup that allows for dual capture of multiple emission bands. However, for this particular study, these issues will not be of major significance.

## 2.2 Extracting membrane and cytoplasmic signal components

Transition to section

### 2.2.1 An overview of existing methods

A number of methods have been implemented aiming to quantify protein concentrations at the membrane and cytoplasm in *C. elegans* embryos. A typical approach to quantify membrane concentrations is to find the region of the image representing the cortex (either by manual or computational segmentation) and take a coarse measure of pixel values within this region (fig. 2.7, *Intensity based quantification*). Such an approach was used by Goehring et al. (2011), who manually segmented the embryo cortex, computationally straightened a region around the circumference of the cell, and defined membrane concentrations as the sum of the highest intensity group of pixels at each cortical cross section. Hubatsch et al. (2019) used a similar approach, but replaced manual segmentation with an automated computational pipeline. Similarly, Zhang et al. (2017) developed a computational protocol to segment images, and defined membrane concentrations around the cell as the average signal intensity within a region representing the cell cortex.

A main disadvantage of these methods is that, as the membrane is immediately apposed to the underlying cytoplasm, pixel values at the membrane will inevitable contain a contribution from cytoplasmic fluorophore signal (and, indeed, cytoplasmic autofluorescence if this isn't accounted for). This means that measurements of membrane concentrations will be sensitive to changes in cytoplasmic concentrations, and means that these methods fail to achieve an

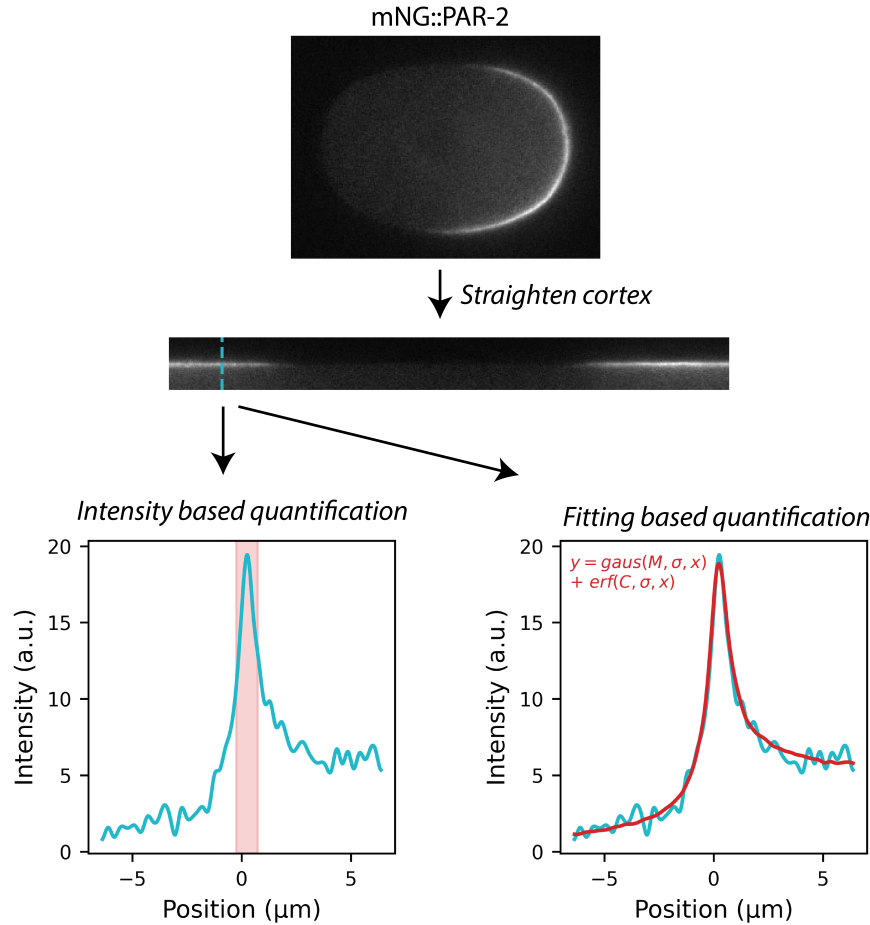


**Figure 2.7: Approaches for quantifying membrane concentrations from midplane images.** Typical methods involve segmentation of embryos, either manually or computationally, followed by computational straightening, to simplify geometry, here shown for an image of mNG::PAR-2. Each position along the x-dimension of the straightened image represents a profile perpendicular to and centred on the membrane at that position. A number of approaches can be used to extract quantitative information from these profiles. Intensity-based methods use pixel values within a central region of the profile representing the membrane (red) as a measure of membrane concentrations. Fitting-based methods fit the shape of the whole profile to a model, and extract relevant parameters from the fitted model. This is shown here for a model based on Gross et al. (2018), which describes total signal as a sum of a Gaussian component representing membrane signal and an error-function component representing cytoplasmic signal. Each component is characterised by an amplitude ( $M$  and  $C$ ) and a shared width parameter ( $\sigma$ ).

accurate zero (a positive signal will always register, even if there is nothing on the membrane). Typically, attempts are made to overcome this latter point by normalising concentrations and/or subtracting away a local or global estimate of the background signal, but this is often difficult and inaccurate.

More advanced methods have aimed to overcome this problem by building models to describe the expected shape of individual cross-cortex profiles, based on summed contributions of cytoplasmic and membrane signal. Membrane and cytoplasmic concentrations can then be extracted by fitting measured profiles to this model, and extracting the relevant parameters describing the amplitudes of the two signal components (fig. 2.7, *Fitting based quantification*). Such an approach was used by Gross et al. (2018), who described the cross-cortex profile at each point around the circumference of the embryo as the sum of a Gaussian and an error-function contribution, representing the expected form of a point (membrane) or step-function (cytoplasm) convolved with a Gaussian-like point spread function in 1D. A similar approach was previously used in Blanchoud et al. (2015) (although with a different description of cytoplasmic signal).

### 2.2.2 Accounting for out-of-focus scatter

Whilst these methods have been effectively deployed in various studies, and are good at capturing a proper zero baseline, their accuracy is inevitably limited by the accuracy of the underlying models. For many imaging set-ups, the assumption that cytoplasmic and membrane contributions can be described by such simple mathematical functions may in fact be far from the truth. This

was demonstrated by for *C. elegans* embryos by Reich (2019), who quantitatively analysed cross-cortex signal in cells containing only cytoplasmic signal, finding that (under imaging conditions similar to those used in this study) the shape of this profile deviates significantly from the expected error-function shape. I have also performed similar analysis here (fig. 2.8), in this case using a line expressing free NeonGreen which is not expected to bind to the membrane, and using SAIBR to remove any autofluorescence contributions. Here we can see the true shape of the cytoplasmic signal contribution, which varies little within embryos (fig. 2.8C) and between embryos (fig. 2.8D).

The main reason that this shape deviates from an error-function is likely due to scattering and diffraction of light from planes above and below the imaging plane, combined with a curved geometry in the z-dimension (fig. 2.9). Scatter, which is a common issue in images of biological samples, causes a broadening of light in three dimensions as it passes through regions of heterogeneous refractive index. This occurs within the (xy) plane of an image, but is typically far more significant in the z-axis. Whilst confocal microscopes are designed to only capture light from a single plane, the whole sample is illuminated, so they will capture any emitted light from other planes that scatters into the focal plane. This means that pixel intensities within the focal plane will be affected not only by structures within that plane but also structures above and below.

It is likely that a similar problem also applies in the case of membrane protein (fig. 2.10). Specifically, this analysis shows that out of focus membrane signal might be expected to lead to a shape resembling an asymmetric Gaussian, with higher signal at the interior of the cell than the exterior. In fact, this phenomenon can be observed just by looking at images of polarised PAR proteins

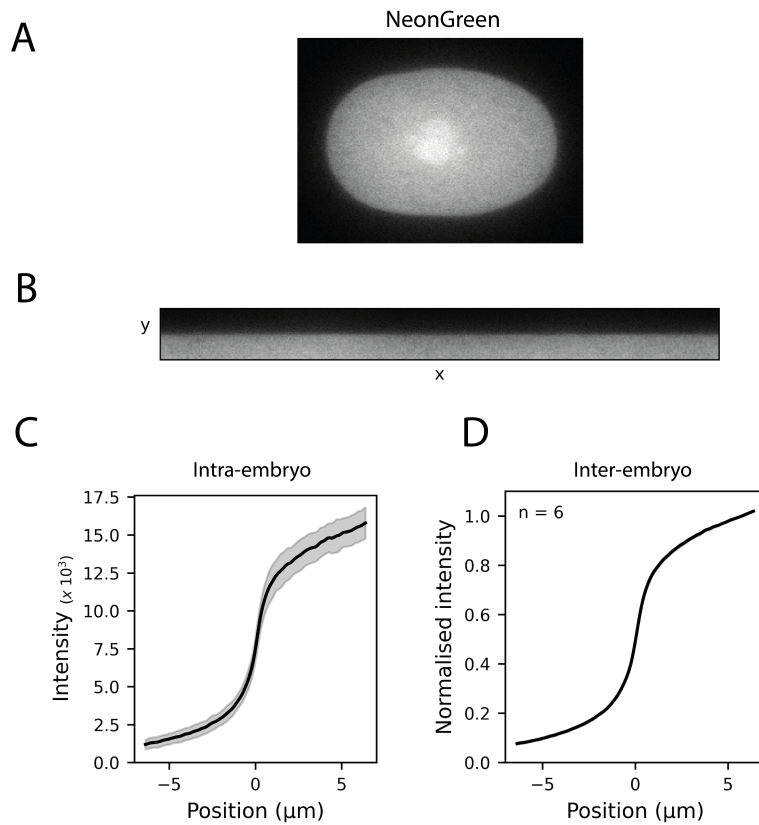


**Figure 2.8: Assessing the contribution of cytoplasmic protein to midplane signal.**  
**(A)** Midplane image of an embryo expressing free NeonGreen. **(B)** Straightened cortex of the image in (A). **(C)** Straightened image in (B), averaged over the x dimension. Mean  $\pm$  SD. **(D)** Mean ( $\pm$  SD) cross-cortex profile, averaged across multiple embryos.

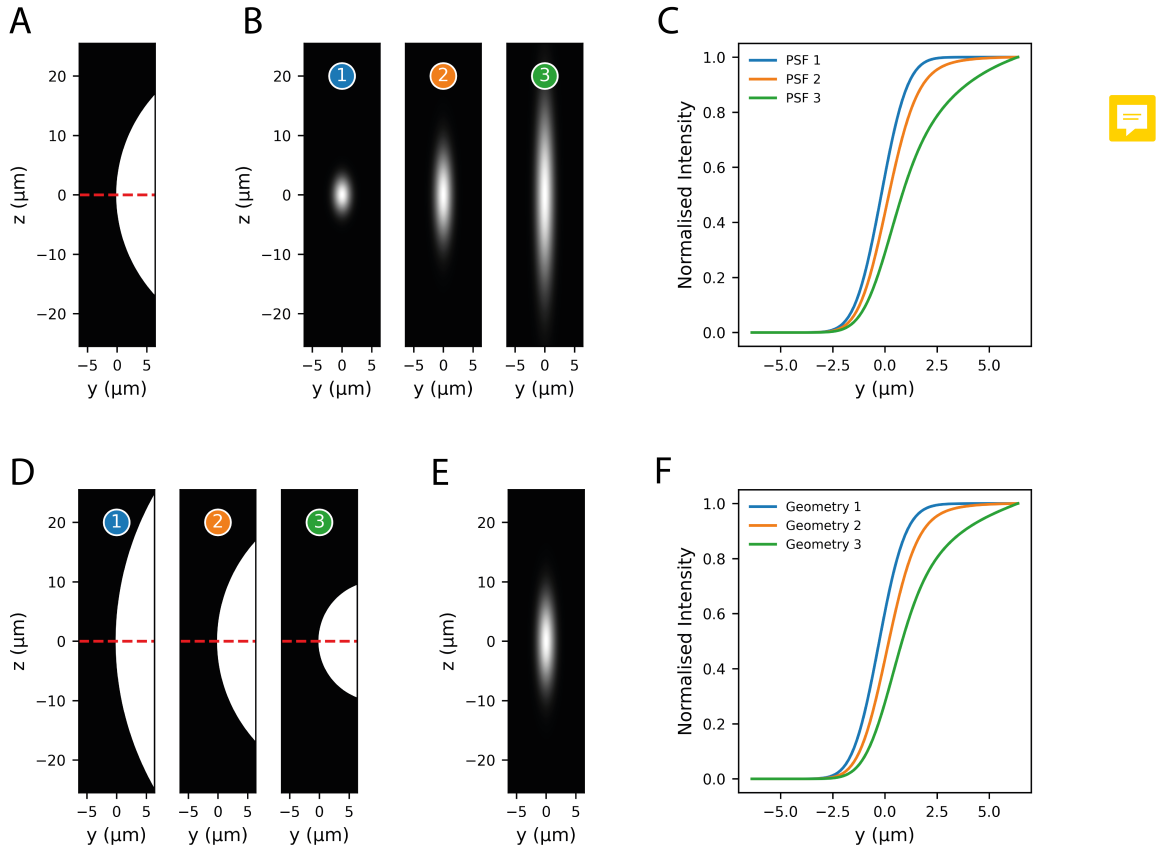


**Figure 2.9: Effects of sample geometry and the PSF on in-plane signal measurements in simulations of cytoplasm-like signal.** (A) - (C) (C) shows simulated midplane signals derived from the geometry shown in (A) convolved with three different point spread functions (B). (D) - (F) (F) shows simulated midplane signals derived from three geometries shown in (D) convolved with the point spread function shown in (E). Geometries are designed to resemble cytoplasmic protein at the edge of a curved cell. Red dashed lines in (A) and (D) indicate midplane. PSFs modelled as 2D Gaussians, which is not representative of real PSFs.

(e.g. fig. 2.7 for PAR-2), where out-of-focus membrane signal can create the appearance of a cytoplasmic gradient. By comparison, two-photon images of PAR-2, which aim to eliminate out of focus excitation, show a completely flat cytoplasm (Petrášek et al., 2008), which is expected for most PAR proteins based on fast measured diffusion rates (PAR-3 and PAR-1 excepting). Whilst in some cases this out-of-focus bleedthrough may be of little concern, it might be particularly problematic if accurate cytoplasmic quantification is required, as this out of focus signal may be attributed to cytoplasmic protein. Without accurate cytoplasmic concentration, measures of membrane to cytoplasmic ratios, which are often used as a read-out of membrane affinity, may be wildly off. This will prove significant for much of the analysis in later chapters of this thesis.

Thus, if we want to obtain accurate measures of cytoplasmic and membrane protein concentrations, we need a method that can account for out-of-focus scatter. One common approach to account for out-of-focus scatter is to take a z-stack across the whole sample and apply a deconvolution algorithm to the 3D stack to reassign all blurred/scattered light to an in-focus location (Wallace, Schaefer, and Swedlow, 2001). These methods rely on prior knowledge of the point spread function (PSF) that applies to the particular sample and imaging set-up, which needs to be as accurate as possible, otherwise artefacts can arise. Theoretical methods exist to estimate an appropriate PSF given parameters such as the imaging modality, numerical aperture and emitted light wavelength. However, whilst these methods are good at describing blur within the imaging apparatus, scattering within the sample and at the sample-apparatus interface is difficult to model accurately. For this reason, it can be more effective to measure an empirical PSF by imaging the 3D light

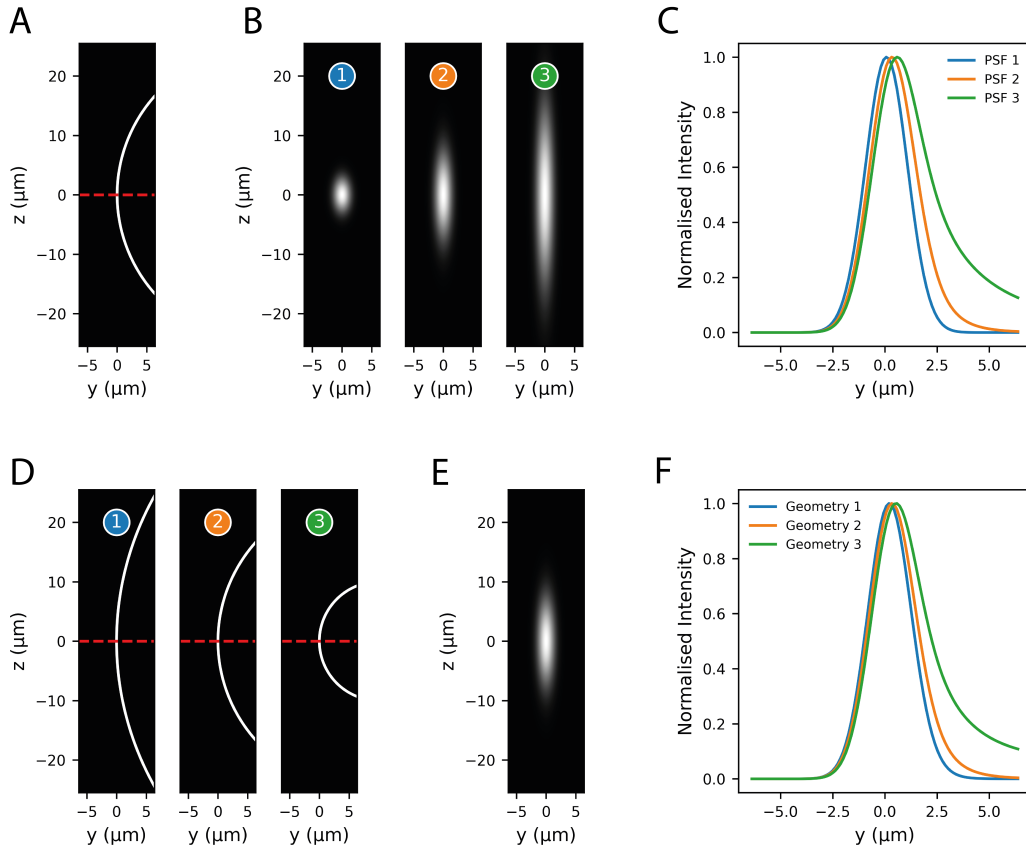


**Figure 2.10: Effects of sample geometry and the PSF on in-plane signal measurements in simulations of membrane-like signal.** (A) - (C) (C) shows simulated midplane signals derived from the geometry shown in (A) convolved with three different point spread functions (B). (D) - (F) (F) shows simulated midplane signals derived from three geometries shown in (D) convolved with the point spread function shown in (E). Geometries are designed to resemble membrane protein at the edge of a curved cell. Red dashed lines in (A) and (D) indicate midplane. PSFs modelled as 2D Gaussians, which is not representative of real PSFs.

distribution from a single point source (e.g. a fluorescent bead) under similar sample prep conditions to the sample of interest. However, as PSFs are influenced by scatter within the sample itself, the accuracy of this method depends on how closely the sample environment can be replicated when imaging the beads, which is not trivial.

Furthermore, most deconvolution methods assume that the PSF is a constant function throughout the whole image, but in many cases this won't be the case. There may, for example, be refractive index gradients within the sample, which will alter the shape of the PSF depending on location within the sample. Additionally, if there is a mismatch between the refractive index of the immersion and mounting media, as is often unavoidable when imaging live biological samples, then the PSF will usually vary with depth as spherical aberrations will be introduced deeper into the sample. A PSF from a fluorescent bead located directly below the coverslip will not capture either of these phenomena.

In reality, given all of these confounding factors, an accurate description of the PSF that applies to a given sample of interest is often unachievable in practice. Whilst deconvolution with a suboptimal PSF may be sufficient for many qualitative applications, accurate quantitative measurements cannot be guaranteed. For this reason, I opted against using a PSF-based deconvolution approach to account for out-of-plane scattering.

Fortunately, in this particular case, matters are simplified by the fact that the geometries of protein distribution are usually highly consistent. Not only is the shape of embryos highly consistent, but PAR protein distributions within the embryo also tend to display rotational symmetry (at least during normal po-

larity development in P0), meaning that protein distributions in planes above and below the focal plane tend to be similar/identical to those seen at the focal plane (much like the simulations in fig. 2.9 and fig. 2.10). Optical properties are also not expected to change from sample to sample, or from location to location around the circumference of an embryo.

Together, these features imply that, in cases where protein is either entirely cytoplasmic or entirely membrane-bound, the normalised shape of the cross-cortex profile measured at the midplane should be some constant function, that shouldn't vary much between embryos or spatially around the circumference of an embryo. A change in local or global concentrations should amount to a rescaling of these profiles, but shouldn't change their normalised shape. Where there is a mix of cytoplasmic and membrane protein, the total measured cross-cortex profile will then be a sum of these two contributions. Therefore, if one has prior knowledge of the expected shape of the cross-cortex profile for cytoplasmic-only and membrane-only protein, then measured profiles can be fit as the sum of these two contributions, and membrane/cytoplasmic concentrations extracted as the amplitudes of the two signal components.

Therefore, a key step in the path to accurate quantification is the ability to measure appropriate reference profiles describing the contributions of cytoplasmic and membrane protein. As mentioned previously, cytoplasmic reference profiles can easily be obtained by analysing cells in which all protein is cytoplasmic (fig. 2.8). Reich (2019) (and Reich et al. (2019)) used an approach half-way between the Gross et al. (2018) method and the method that I am proposing, replacing the error-function description of cytoplasmic signal with a measured cytoplasmic reference profile. Thus, total signals were fit as the

sum of a Gaussian profile and this reference profile, which resulted in a better ability of the model to fit the shape of measured profiles.

Whilst this move is a significant step in the right direction, the problem remains of how best to account for out of focus membrane light. This presents a challenge: whilst it is relatively easy to directly measure a cytoplasmic reference profile (you just need a reference image in which all signal is cytoplasmic), the same is not true for a membrane profile as it is difficult to find a reference case in which all protein is membrane bound. To extend the method to account for out-of-focus membrane protein, I attempted to find alternative methods to get an approximation of the membrane reference profile. An initial idea, which involved staining the exterior of the embryo eggshell with a fluorescent dye, proved technically challenging and not reproducible.

Instead, the problem becomes simplified when one considers that, even in cases where the membrane is polarised, the cytoplasmic pool of most PAR proteins should be uniform (although exceptions do exist in the case of PAR-1 and PAR-3, where true cytoplasmic gradients have been observed). Thus, straightened cortices can be modelled as a uniform cytoplasmic component, defined by a cytoplasmic reference profile ( $R_c$ ) and a single, uniform, cytoplasmic concentration ( $C$ ), plus a polarised membrane component, defined by a membrane reference profile ( $R_m$ ) and a nonuniform membrane concentration profile ( $M$ ), as shown in fig. 2.11. This is essentially a generalisation of the *Fitting based quantification* method presented in fig. 2.7, but proposes the use of arbitrary membrane and cytoplasmic reference profiles rather than mathematical functions (e.g. Gaussian, error function), and has the restriction of a uniform cytoplasm.

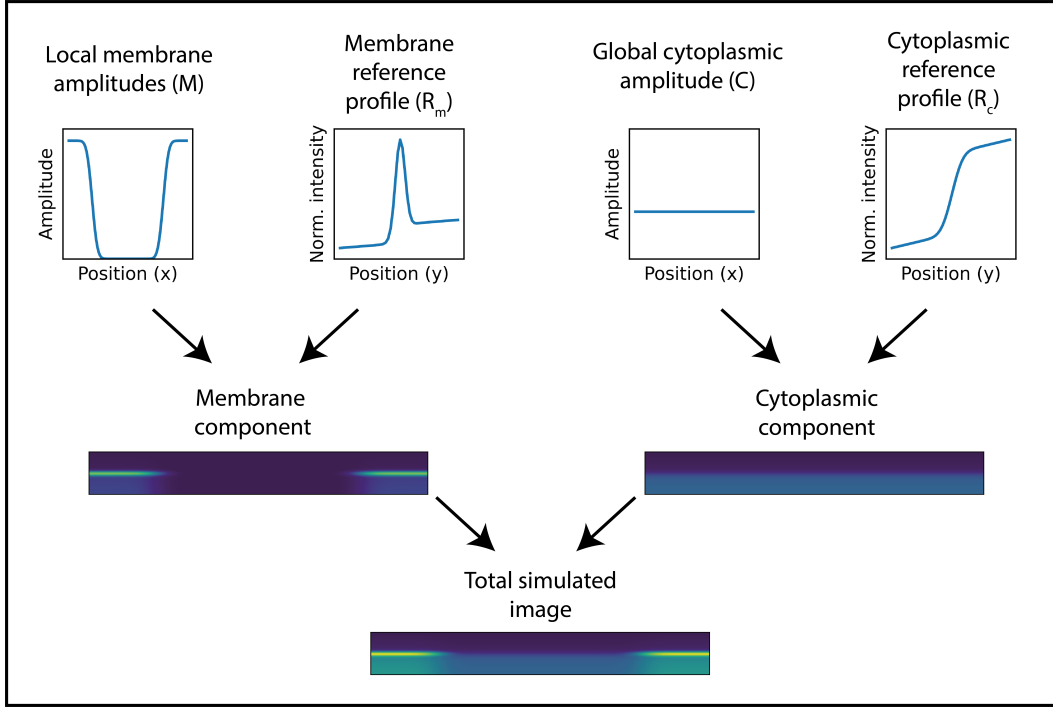


**Figure 2.11: A model for simulating membrane and cytoplasmic fluorescence signal at the cortex.** Simulated images of straightened cortices are described as the sum of membrane and cytoplasmic signal components. The membrane component is described as a 1D array of amplitudes ( $M$ ), representing concentrations around the circumference of the embryo, convolved with a membrane reference profile ( $R_m$ ). The cytoplasmic component is described as a single uniform amplitude ( $C$ ) convolved with a cytoplasmic reference profile ( $R_c$ ). Blur/scatter in the  $x$  dimension is ignored as adjacent positions are assumed to be similar.

$R_c$  can easily be predefined by imaging embryos in which all protein is cytoplasmic (fig. 2.8). If we assume for now that  $R_m$  is also predefined, then  $M$  and  $C$  for a given embryo can be determined by fitting a straightened image to the model presented in fig. 2.11. (At this point concentrations will be in arbitrary units, but I'll return to this point later). Whilst  $R_m$  is in fact not predefined, given the constraints imposed by cytoplasmic uniformity, only a model with an appropriate  $R_m$  will be able to create simulated images that closely match experimental images. (Imagine, for example a model with a Gaussian

membrane reference profile, which would clearly fail to capture graded interior signal). Therefore, under conditions such as these, in which we have a uniform cytoplasmic component and a graded membrane component,  $R_m$  need not be predefined, and can simply be fit to the data along with the concentration parameters. To perform this kind of optimisation, I have developed a gradient descent approach based on differentiable programming, which I describe below.

### 2.2.3 A gradient descent protocol for image quantification

Gradient descent is a popular optimisation strategy used for a number of machine learning applications. When optimising a model described by a series of parameters, the idea of gradient descent is to calculate the partial derivative of each parameter with respect to a loss term (e.g. mean squared error). A negative gradient for a certain parameter would imply that an increase in that parameter would decrease the loss term, whereas a positive gradient would imply the opposite. Therefore, to reduce loss, each input parameter can be adjusted in proportion to the negative of its partial derivative. Starting with a set of initial conditions, this procedure is iteratively repeated, adjusting parameters and calculating new gradients at each step, until the loss term reaches a minimum.

The utility of these methods has been greatly advanced in recent years by the development of differentiable programming tools. Commonly used for deep learning, although generalisable to other problems, these tools greatly speed up computation for complex optimisation procedures by automatically calculating gradients, rather than relying on numerical methods, using a pro-

cess known as backpropagation. In addition, extensions to the basic gradient descent algorithm have proven effective at speeding up convergence and preventing entrapment in local minima (Sun et al., 2019).

In the case of this particular problem, the procedure is described in fig. 2.12. Given a set of parameters ( $M$ ,  $C$ ,  $R_m$ ,  $R_c$ ), a forward propagation step simulates an image, and this is compared to the ground truth image to calculate a loss term. Backpropagation then calculates the gradient of each of the input parameters with respect to this loss term. At this point, we can adjust some or all of the input parameters according to these gradients. Repeating this cycle of forward and back propagation will then lead to a gradual optimisation of these parameters, until the loss function reaches a minimum.

To test this approach, I built a model using the differentiable programming package Tensorflow (Abadi et al., 2016), and first applied it to images of polarised PAR-2. The model was initiated with all concentrations ( $M$  and  $C$ ) equal to zero, and  $R_m$  initiated as a Gaussian. For  $R_c$  I used a measured profile (fig. 2.8), and this was not adjusted during training (fig. 2.13A). Using an Adam optimiser (Kingma and Ba, 2015) with a learning rate of 0.01, all other parameters ( $M$ ,  $C$  and  $R_m$ ) were then adjusted iteratively until a plateau was reached (250 steps), as shown in fig. 2.13B. The final simulated image, composed of a uniform cytoplasmic component and a nonuniform membrane component, closely matches the ground truth image (fig. 2.13C).

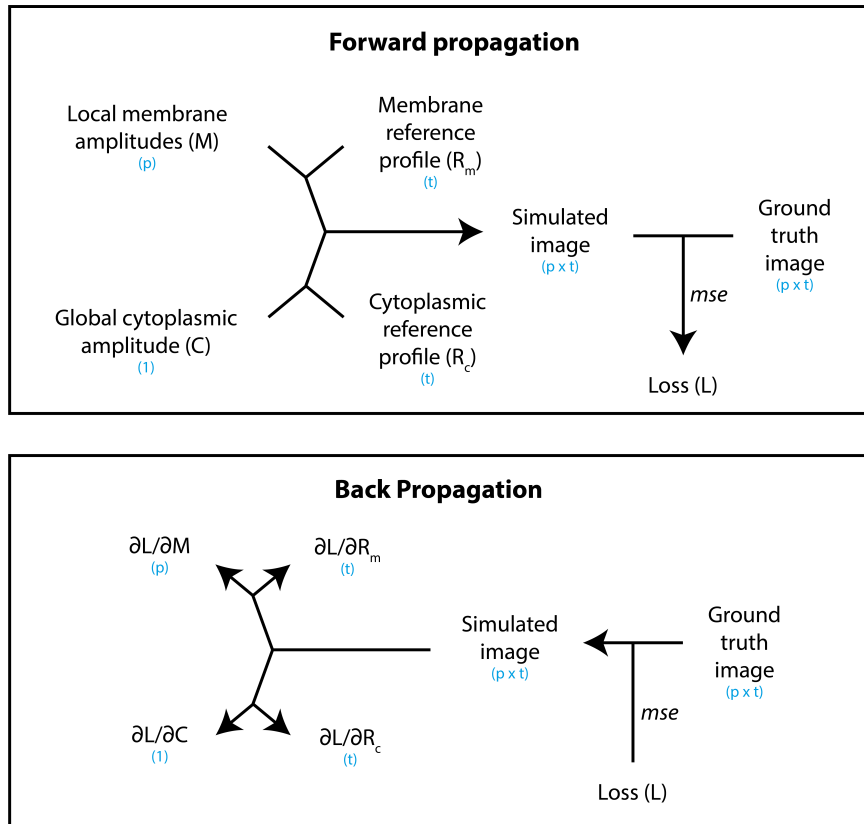


**Figure 2.12: Backpropagation gradient descent protocol for parameter optimisation.** Parameters are optimised by an iterative cycle of forward and back propagation. In the forward propagation step (top), an image is simulated given input parameters  $M$ ,  $C$ ,  $R_m$ ,  $R_c$ , and compared to the ground truth image to calculate a loss term. In the back propagation step (bottom) gradients of the loss term with respect to each of the input parameters are calculated using the chain rule method. A subset of the input parameters can then be changed according to these gradients, which will depend on the procedure (e.g. fig. 2.13 vs fig. 2.15). This process is repeated many times until optimisation reaches a plateau. Dimensions of the variables are shown in blue, where  $p$  represents the number of positions to fit around the cortex, and  $t$  represents the thickness of the straightened image.

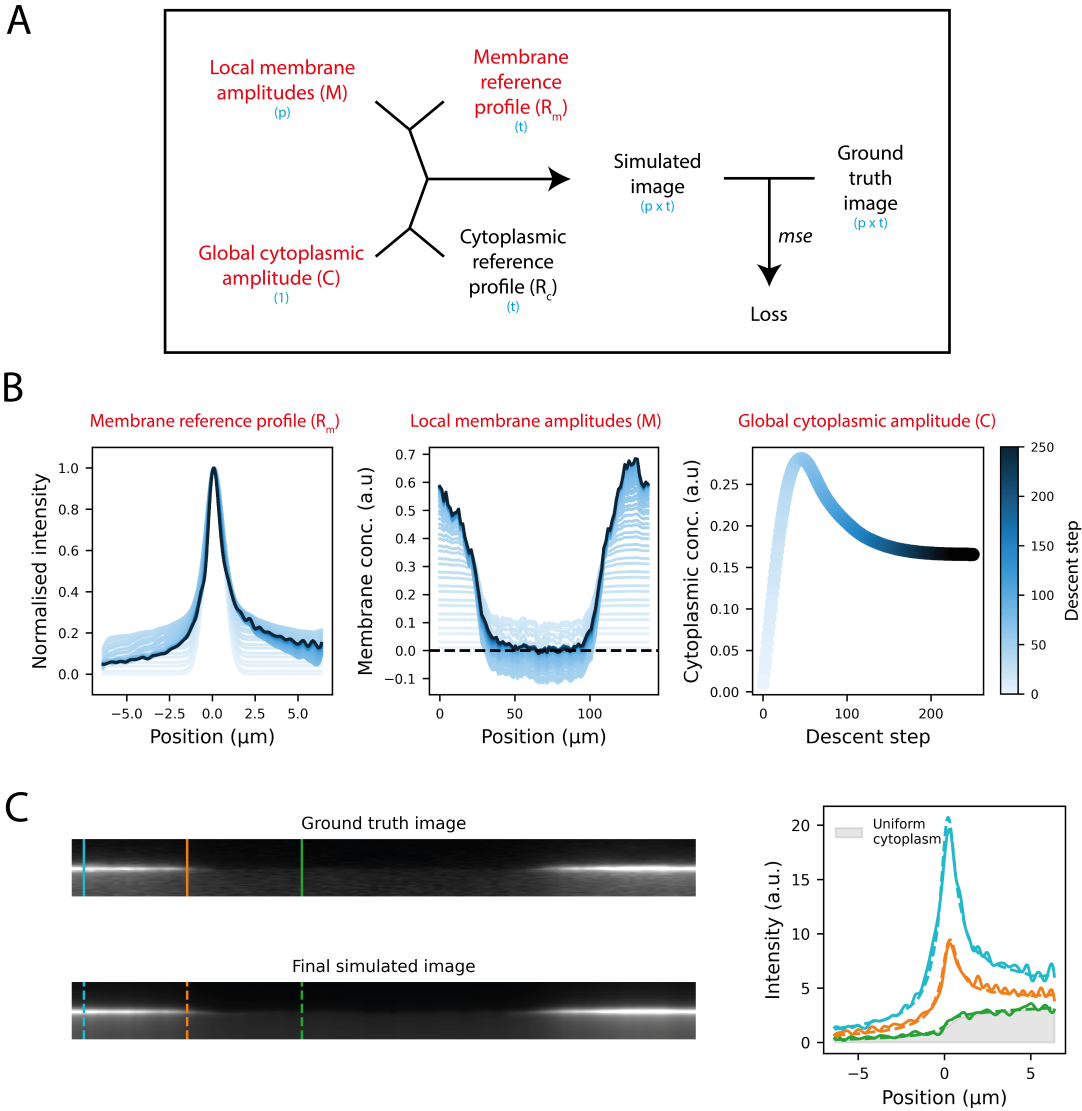


**Figure 2.13: Separation of membrane and cytoplasmic signal in an image of mNG::PAR-2.** (A) Schematic demonstrating the optimisation procedure, highlighting the input parameters to be optimised in red. (B)  $R_m$ ,  $M$  and  $C$  throughout the training procedure for an mNG::PAR-2 expressing polarised embryo.  $R_m$  was initiated as a Gaussian (radius =  $x$ ) centred at zero,  $M$  and  $C$  initiated as zero. (C) Final simulated image compared to the ground truth image. Right panel shows profiles at specified positions (solid = ground truth, dashed = simulated). Uniform cytoplasmic component shared between profiles indicated in gray.

#### 2.2.4 Segmentation

In addition to the parameters already mentioned, the full model also includes a series of alignment parameters, which can also be trained by gradient descent, allowing the model to freely align to the data in the y direction. As a result, ground truth images do not need to be accurately segmented prior to optimisation, and rough manual ROIs are fine to use. This is particularly useful for timelapse movies, where, even if the embryo undergoes shape changes, only a single manual ROI needs to be provided. An additional outcome of alignment is that the offset parameters can be used to refine the original ROI, meaning that the method can serve as a tool for computational segmentation. Refined ROIs can then be used to re-straighten the cortex, and optimisation repeated (fig. 2.14). Overall, this allows cortices to be segmented with subpixel accuracy with minimal manual input. In theory, the initial manual step could also be automated using deep learning methods to create a fully automated pipeline (**Minaee2021**).

#### 2.2.5 Benchmarking the method

The method described so far is limited to cases of images with polarised membranes. However, as discussed previously,  $R_m$ , which is a function of local geometry and optical properties, should be a constant function applicable to all embryos. Therefore, much like I used a predefined  $R_c$  when fitting images of polarised PAR-2, images of proteins without a polarised membrane can be quantified by using an  $R_m$  derived from a calibration procedure on polarised images.

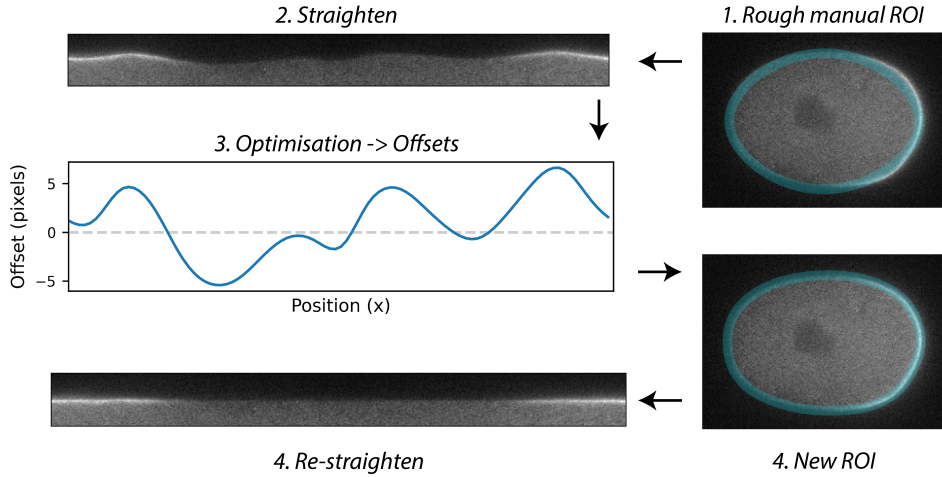


**Figure 2.14: Semi-automated segmentation algorithm.** Segmentation is initiated with a rough manual ROI. The cortex is then straightened and fit to the model yielding, among other parameters, parameters describing offset at each position along the x dimension. These offsets can then be used to adjust the initial ROI, and re-straighten the cortex. The re-straightened cortex can then be refit to the model to give concentration parameters. Shown here for an embryo expressing mNG::PAR-2(L109R).

To test this method, I performed quantification on images of embryos expressing the uniform plasma membrane probe GFP::PH with variable expression levels (fig. 2.15B), obtained by performing an RNAi rundown using XFP RNAi feeding bacteria (see Methods). In this case, I used a predefined  $R_m$  and  $R_c$ , and only optimised  $M$  and  $C$  (as well as the alignment parameters described in the previous section) (fig. 2.15A). Images were initiated with a rough manual ROI and segmented using the method described in fig. 2.14 prior to final quantification. Compatible with expected linear membrane binding kinetics, we can see that the method gives a tight linear relationship between cytoplasmic and membrane concentrations (fig. 2.15C). N2s are also accurately described as having cytoplasmic and membrane concentrations close to zero.

I next investigated how robust the pipeline is to changing signal-to-noise ra-

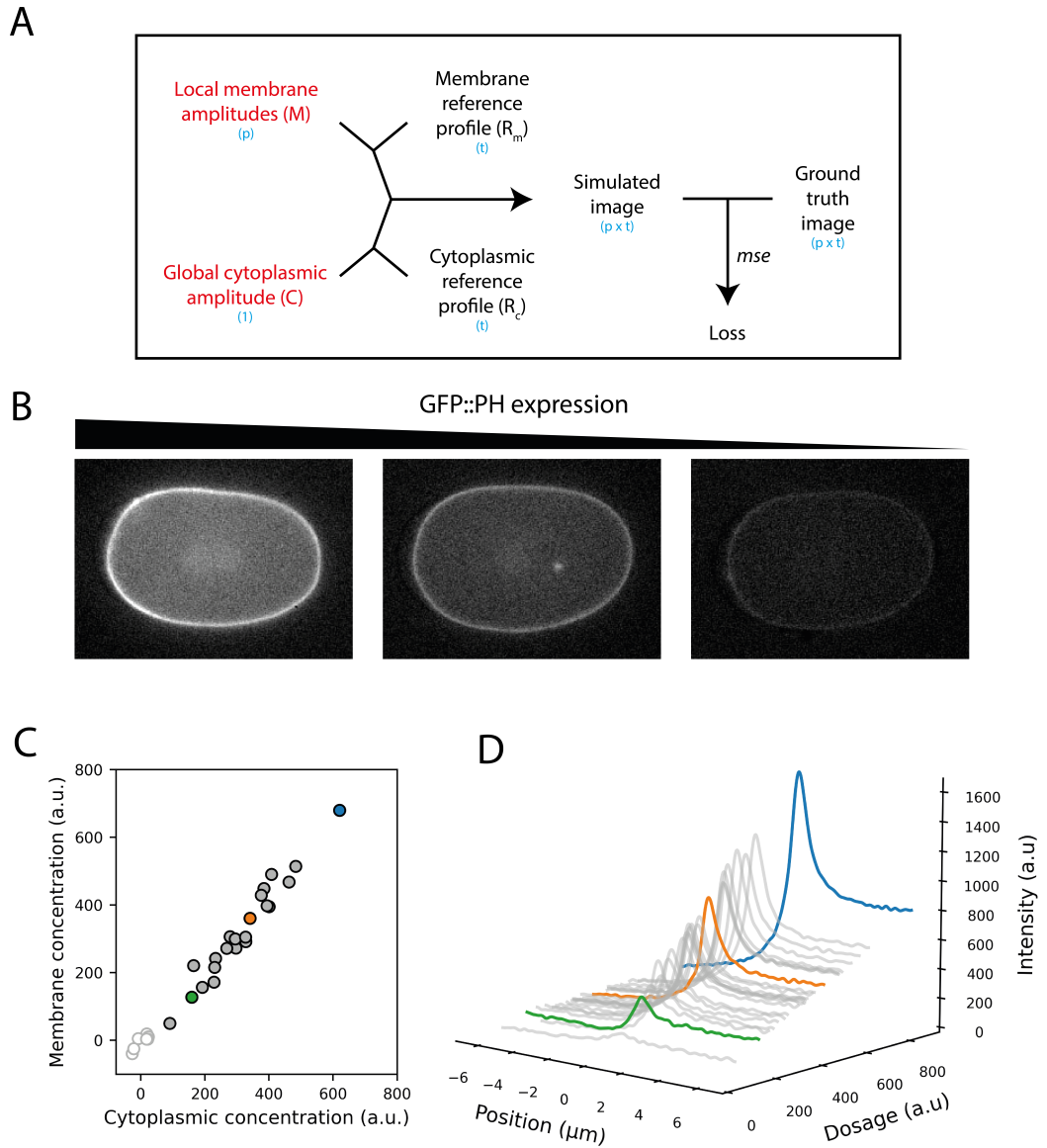


**Figure 2.15: Quantification of GFP::PH expressing embryos reveals a linear relationship between membrane and cytoplasmic concentrations.** (A) Schematic demonstrating the optimisation procedure, highlighting the input parameters to be optimised in red. (B) Images of GFP::PH expressing embryos with varying dosages of GFP::PH, obtained by RNAi rundown. (C) Membrane vs. cytoplasmic concentrations for the full dataset of embryos. Empty circles represent untagged N2 embryos. Embryos in (B) represented by blue, orange and green circles. (D) Cross-cortex profiles averaged over the entire circumference of the embryo vs. GFP::PH dosage. Colour coding as in (C).

tios, using images of three GFP::PH embryos with varying expression levels and adding varying levels of Gaussian pixel noise (fig. 2.16A). As seen in fig. 2.16B and C, pixel noise adds noise to the resulting quantifications, but doesn't bias the data in any direction. Quantification of untagged N2s is also not biased by noise (fig. 2.16B/C grey points).

## 2.2.6 Calibrating concentration units

As  $M$  and  $C$  are in arbitrary units (effectively in units of their own respective reference profiles), a conversion parameter, is required to put them into common units. To calibrate this conversion parameter, I quantified the effects on  $M$  and  $C$  measurements of redistributing a fixed pool of protein from the cytoplasm to the membrane. To do this, I used an optogenetics system with a plasma membrane bound PH::eGFP::LOV to move a cytoplasmic pool of ePDZ::mCherry to the membrane (Fielmich et al., 2018). Embryos were exposed to blue light for 10 seconds, which promotes binding between ePDZ and LOV, leading to a rapid uniform recruitment of ePDZ::mCherry to the membrane and a reduction in the concentration in the cytoplasm (fig. 2.17). Where ePDZ::mcherry is expressed alone, this localisation shift isn't observed (fig. 2.17, grey points).

Whilst there is significant protein relocalisation in the optogenetic system, the total amount of protein before and after blue light exposure can be assumed to be constant. This total amount,  $T$ , can be expressed as the  $C$  value that would be expected if all tagged molecules were in the cytoplasm, given by equation 1 where  $\psi$  is the surface-area to volume ratio of the cell ( $= 0.174\mu m^{-1}$  (Goehring

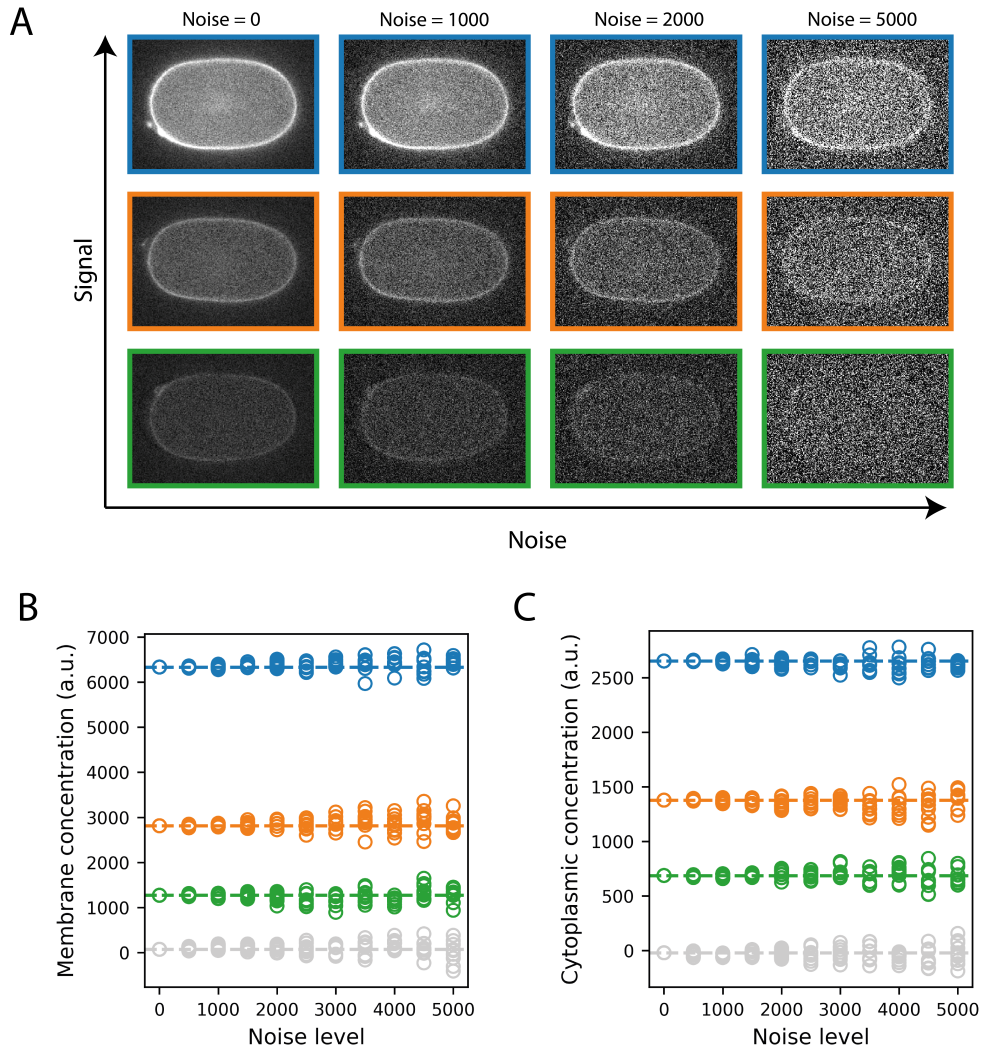


**Figure 2.16: Quantifications of membrane and cytoplasmic concentrations are robust to pixel-noise.** (A) Images of three GFP::PH expressing embryos with varying amounts of GFP::PH subject to varying levels of Gaussian pixel noise. (B) Quantifications of membrane concentration (averaged over the entire embryo) for the three embryos in (A) subject to varying levels of pixel noise, colour coded by embryo. For each noise level 10 images were generated for each embryo, and each images was quantified and plot as a single point. Similar analysis for an untagged N2 embryo is also shown (gray). Dashed lines indicate quantification at noise=0. (C) Quantifications of cytoplasmic concentration for the three embryos in (A) and a single N2 embryo subject to varying levels of pixel noise. Procedure as in (B). Noise level defined as standard deviation of Gaussian noise added to the image.

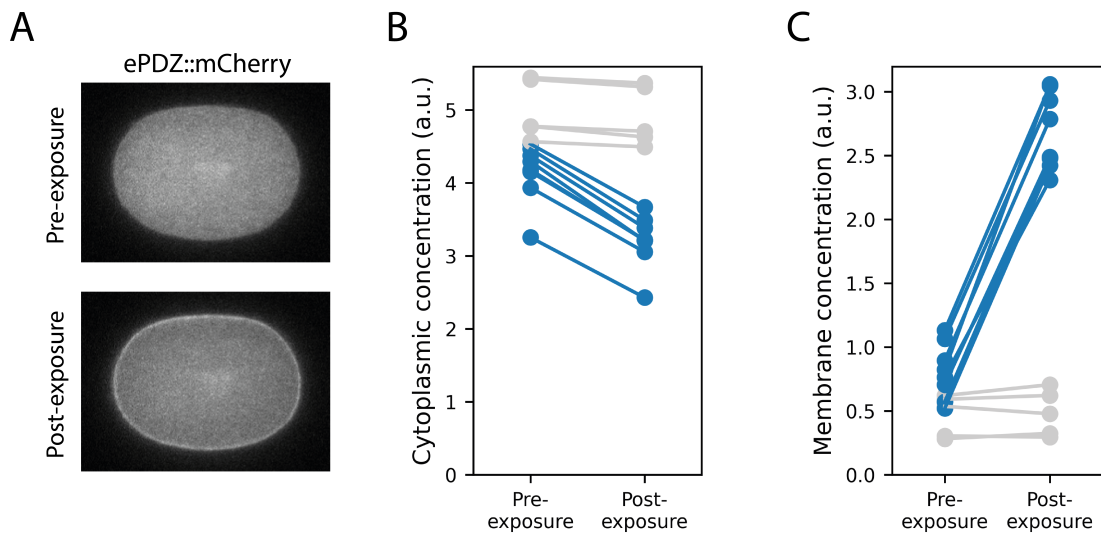


**Figure 2.17: Redistribution of fluorescent signal from cytoplasm to membrane using optogenetics.** (A) ePDZ::mCherry before (top) and after (bottom) exposure to blue light, in an embryo also expressing PH::eGFP::LOV. (B) Cytoplasmic concentration of ePDZ::mCherry (in arbitrary units) before and after blue light exposure for embryos with (blue) and without (gray) PH::eGFP::LOV. (C) Membrane concentration of ePDZ::mCherry (in arbitrary units) before and after blue light exposure for embryos with (blue) and without (gray) PH::eGFP::LOV.

et al., [2011]). Given that  $M$  is in different arbitrary units to  $C$ , a conversion parameter,  $c$ , is required:

$$T = C + \psi c M \quad (1)$$

Given that  $T$  is the same before and after exposure,  $c$  can be calculated, on an embryo by embryo basis, by comparing the gain in  $M$  post-exposure to the loss in  $C$ :

$$c = \frac{C_{\text{pre-exposure}} - C_{\text{post-exposure}}}{\psi(M_{\text{post-exposure}} - M_{\text{pre-exposure}})} \quad (2)$$

Performing this analysis on the dataset in fig. 2.17 (blue points) gives a value of  $c = 2.88 \pm 0.12 \mu\text{m}$  (mean  $\pm$  SD), which can be used to convert membrane concentrations to the same common units as cytoplasmic concentrations (i.e.  $\mu\text{m}^{-3}$  for cytoplasmic concentrations and  $\mu\text{m}^{-2}$  for membrane concentrations). Note that these concentrations are still arbitrary in the sense that they do not indicate absolute concentrations (i.e. absolute number of molecules per unit area). However, for much of the analysis in the following sections, where the aim is to measure membrane affinities (membrane to cytoplasmic ratios) this will not be an issue, although I'll return to this point in section x.

### 2.2.7 Discussion

Accurate quantification of features from images relies on the ability to separate overlapping signals and correctly attribute signals to their source. In this section, I have described a two-step pipeline designed for accurate quantification of cytoplasmic and membrane concentrations from midplane images of *C. elegans* zygotes. The first step involves separation of autofluorescence and fluorophore signal, and the second step involves separation of signals from cytoplasmic and membrane protein. The overall pipeline is not specific for any particular microscope, and makes no assumptions about the spectral characteristics of the signal components or the optical properties of the imaging system/sample. Whilst the SAIBR method isn't fundamentally tied to *C. elegans*, and has been shown to apply to other systems, the method for separation of cytoplasmic and membrane signals is less generalisable, and a number of assumptions in the model presented here are firmly linked to the simple and reproducible geometries of *C. elegans* zygotes and PAR protein patterns. Nevertheless, the ability to confidently quantify relative membrane and cytoplasmic concentrations *in vivo* brings forward new experimental possibilities for studies of the *C. elegans* PAR network, and will prove fundamental to much of the work presented in the following chapters of this thesis.